

## Research Article

# Transonic Static Aeroelastic Numerical Analysis of Flexible Complex Configuration Wing

Changrong Zhang , Hongtao Guo , Binbin Lv , Jun Zha , and Li Yu 

*Institute of High Speed Aerodynamics, China Aerodynamics Research & Development Center, Beichuan 622763, Sichuan, China*

Correspondence should be addressed to Hongtao Guo; ght@cardc.cc

Received 10 January 2021; Revised 5 April 2021; Accepted 10 April 2021; Published 20 April 2021

Academic Editor: Zeqi Lu

Copyright © 2021 Changrong Zhang et al. This is an open access article distributed under the Creative Commons Attribution License, which permits unrestricted use, distribution, and reproduction in any medium, provided the original work is properly cited.

Diamond back wing is subjected to large deformation while gliding, which significantly changes characteristics of the lift as well as the static stability. For this reason, conventional rigid aircraft assumption cannot meet the requirements of the aerodynamic analysis of such aircrafts for accuracy. In this paper, based on CFD/CSD methods, the static aeroelasticity of a small diameter bomb with diamond back wing was studied. The results showed that static aeroelastic effects cause the slope of lift line to drop by 21% and the aerodynamic centre to move backwards by a 1.5% bomb body length, which will deviate the actual flight performance from the design point, thereby decreasing the cruise efficiency and the cruise range.

## 1. Introduction

As illustrated in Figure 1, diamond back missile wing is a gliding range extended component which has been successfully applied to the American small diameter bomb (SDB) GBU-39 USA and the Chinese Feiteng series guided bomb. The SDB diamond back wing has a compact structure and can be installed in a small embedded bomb cabin. After unfolding the back-extended component, it can be launched outside the defense area with a larger gliding range. Considering its advantages of high lift-to-drag ratio and strong ability of gliding, its stiffness and strength of high-aspect-ratio wing can be increased to avoid flutter [1]. In order to reduce the resistance and installation space, the thickness of the front and rear wings of diamond backed projectile wing is small while its aspect ratio is large for the purpose of high lift-to-drag ratio. This however would lead to a large aeroelastic deformation when it glides. The aerodynamic load of the projectile wings differs significantly from that of the original shape, which greatly affects the aerodynamic characteristics of the whole projectile.

The classical static aeroelastic analysis method adopts the hypothesis of potential flow theory and thus is unable to predict the nonlinear phenomena such as shock wave flow

separation in transonic region. The computational fluid dynamic (CFD) and computational structural mechanics (CSD) make it possible to accurately calculate aeroelastic problems by coupling CFD and CSD [2–11]. The coupling methods of CFD and CSD are generally divided into tight coupling and loose coupling.

The tight coupling method can simultaneously solve the fluid control equation and structural dynamic equation in each internal time step and can simulate the real situation. However, it costs a lot of computing resources, and it is still difficult to use this method to solve the complex three-dimensional problems in engineering applications. The loose coupling method solves the fluid dynamic and structural dynamics equations separately and can apply the existing aerodynamic and structural solution modules. It needs to exchange the data of the aerodynamic/structural interface at an appropriate time point and iterate repeatedly until the solution converges. The method can be applied to the static aeroelastic calculation without time variables [12–16].

There are extensive foreign and domestic studies on folding and connecting wing [17–19] and aerodynamic characteristics and layout optimization design of diamond back projectile wing [20,21]. Nevertheless, few of them are regarding the static aeroelastic effect of diamond back



FIGURE 1: Sketch of small diameter bomb with diamond back wing.

projectile wing, and they are still in the infancy [22–25]. In this paper, the static aeroelastic numerical simulation of a diamond back SDB is realized by the coupling of RANS equation and the static equilibrium equation and combining the structured dynamic grid with multifield data interpolation technology. The affection of static aeroelasticity on the geometric deformation characteristics, surface pressure distribution, and aerodynamic performance of the diamond back projectile wing are analyzed based on the numerical simulation results.

## 2. Computing Method

**2.1. CFD Governing Equations.** The governing equation is a time-dependent, three-dimensional conservation compressible RANS equation. In the curvilinear coordinate system ( $\xi$ ,  $\eta$ , and  $\zeta$ ), its dimensionless form is expressed as follows:

$$\frac{\partial Q}{\partial t} + \frac{\partial(F - F_v)}{\partial \xi} + \frac{\partial(G - G_v)}{\partial \eta} + \frac{\partial(H - H_v)}{\partial \zeta} = 0, \quad (1)$$

where  $t$  is time,  $Q$  is conservation variable,  $F$ ,  $G$ , and  $H$  are inviscid vector flux, and  $F_v$ ,  $G_v$ , and  $H_v$  are viscous vector flux.

The S-A model of equation (1) is applied to turbulence simulation. The body surface is adiabatic sliding free boundary condition, the boundary condition of far field is pressure free, and the multigrid technology is applied to accelerate the computational convergence of CFD.

**2.2. CSD Governing Equation.** The structural elastic equilibrium equation is applied to solve the elastic deformation of the structure. The calculation equation is

$$u_s = CF_s, \quad (2)$$

where  $C$  is the flexibility matrix,  $u_s$  is the deformation displacement of the structural finite element node, and  $F_s$  is the column vector of external load which acts on the structural points.

**2.3. Interpolation Method for Fluid Structure Coupling Data.** When CFD and CSD are coupled to solve nonlinear aeroelastic problems, data exchange is required on the coupling

surface of aerodynamic structure. The aerodynamic force obtained by the aerodynamic calculation is applied to the structural nodes, and the structure is subjected to deformation. The displacement of the structural nodes should be fed back to the aerodynamic grid nodes. Considering the calculation efficiency and interpolation accuracy, the three-dimensional thin plate spline interpolation method (TPSI) is adopted in this paper. The calculation method of TPSI can be found in [26–28].

**2.4. Generation Method for Dynamic Mesh.** This paper combines RBF and TFI method to generate dynamic grid. The RBF can be regarded as a three-dimensional extension of the surface spline interpolation method [29]. Its interpolation formula is expressed as

$$f(r) = \sum_{i=1}^n a_i \varphi(\|r - r_i\|) + \psi(r), \quad (3)$$

where  $r_i = (x_i, y_i, z_i)$  is the coordinates of the point whose displacement is known and number is  $n$  and  $\varphi$  is the basic function of the displacement  $\|r - r_i\|$ . In this paper,  $\varphi\|r - r_i\| = \|r - r_i\|^3$  and  $\psi = b_0 + b_1x + b_2y + b_3z$ , and the coefficients of the interpolation formula can be obtained by the displacement and equilibrium conditions of the known points.

Based on the mesh block surface, the displacements of the points in the mesh block can be obtained by TFI interpolation. Similarly, the displacements of the points on the edge of each grid block are obtained by the RBF method [30].

## 3. Calculation and Verification

**3.1. Calculation Process.** Static aeroelastic calculation is an iterative process of CFD/CSD. The flowchart of loose coupling method is presented in Figure 2. The topological structure and the number of grids will not change during the calculation. Thus, the CFD calculation results of the previous deformation step can be applied to the next step as the initial value, and the iteration step of CFD calculation can be decreased. In general, the computational results tend to convergence with 6–7 iteration steps which is 1.5 to 2 times to its rigid CFD counterpart [31–33].

**3.2. Calculation Model.** In this paper, the numerical calculation of the static aeroelastic for a diamond back SDB is carried out, and the results are compared with the wind tunnel test results. The projectile wing combines the high-aspect ratio with the layout scheme of “x” tail rudder. Figure 3 shows the calculation grid near the rigid bomb wing surface. There are about 16.5 million space grid elements of the whole bomb in total.

The structure diagram of the diamond back projectile wing is shown in Figure 4. The chord length of the front wing is 23 mm, and the sweptback angle is 30 degrees; the chord length of the rear wing is 21 mm, and the forward-swept angle is 10 degrees. The distance between the front and rear wings is 145 mm, and the half span length is 200 mm. In

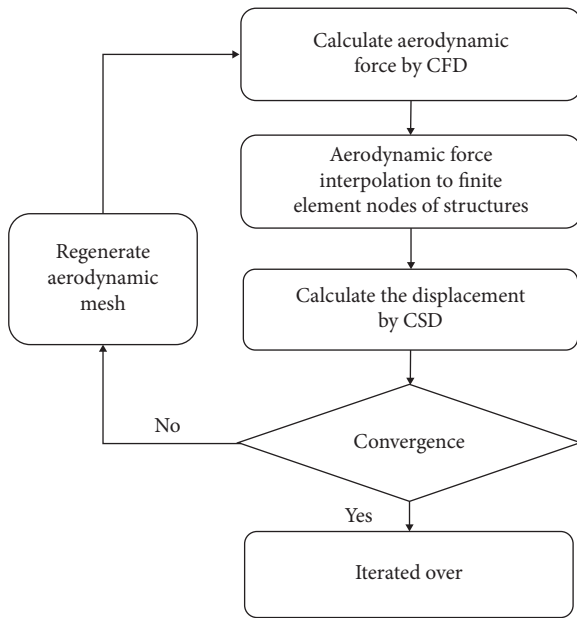


FIGURE 2: Loose coupling flowchart.

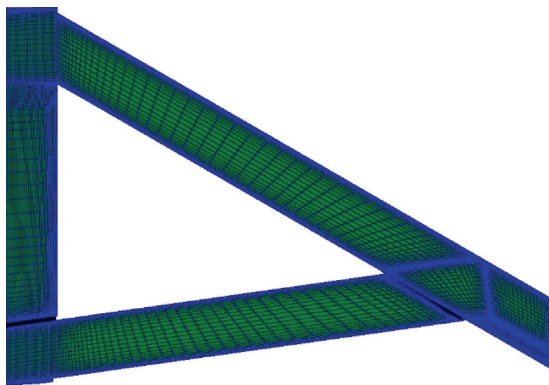


FIGURE 3: Surface mesh on diamond back wing.

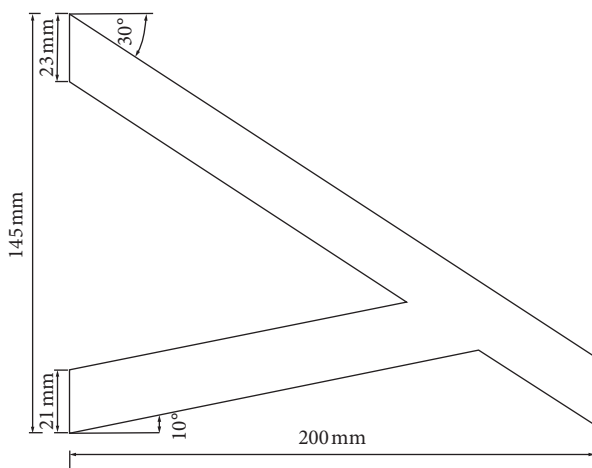


FIGURE 4: Sketch of diamond back wing.

order to improve the aerodynamic performance, a supercritical airfoil with a relative thickness of 10% is adopted to the diamond back projectile wing, and the installation angles of front and rear wings are 2.5 degrees. The flexibility matrix is obtained by the commercial software, and the material of the whole bomb adopts 45-type steel.

**3.3. Verification of Calculation Method.** The parameters of the verification sample are set as follows:  $Ma = 0.8$ ,  $H = 0$  km, and the attack angle ranges from  $0^\circ$  to  $4^\circ$ . The displacement convergence process of the front wing is shown in Figure 5. It can be seen that the deformation of the wing tends to converge with a few iteration steps.

The calculation results are compared with the wind tunnel test results. The comparison results of coefficient for lift force  $C_L$ , pitching moment  $C_m$ , and bending deformation are shown in Figure 6, which are consistent with the experimental results. As shown in Figure 6, both the calculation results of  $C_m$  and the bending trend of the front and rear wing are consistent with the experimental results, and the error is less than 2 mm in all spanwise section. The calculated bending displacement curve is smoother than the experimental one. And, this difference may be attributed to the measurement error of measuring equipment. The difference of  $C_L$  appears when airflow separation occurs at the larger angle of attack on the airfoil. The reason lies in two aspects. One is the insufficient simulation of turbulence and the inaccurate simulation of flow separation characteristics caused by the RANS equation that the current CFD calculation follows. The second is that the CSD calculation uses the structural statics balance equation based on the linearization theory; but, in actual situations, the airfoil will have structural geometric nonlinearity under heavy loads.

## 4. Analysis of Calculation Results

To obtain a large lift-to-drag ratio, the SDB diamond back projective wing has a large aspect ratio and adopts supercritical airfoil with a relatively small thickness. At transonic speed, the viscous effect should not be ignored due to the strong interaction between shock wave and boundary layer, though the angle of attack is very small. It is therefore necessary to calculate the aerodynamic force by N-S equation. In general, this paper focuses on the static aeroelastic characteristics of the sample model with the parameters of  $Ma = 0.8$  and  $H = 0$  km.

**4.1. Effect of Geometric Deformation.** The variation curves of  $\Delta z$  and  $\Delta \varepsilon$  (elastic torsion angle) of the front and rear wings along the spanwise are shown in Figure 7, where  $Ma = 0.8$ ,  $H = 0$  km, and  $\alpha = [-8^\circ \sim 8^\circ]$ . From Figure 7, it can be seen that the calculation boundary is  $\alpha = -4^\circ$ . When the value of  $\alpha$  is larger than  $-4^\circ$ , the static aeroelastic effect makes the front and rear wings produce bending deformation along the spanwise direction and produce a negative elastic torsion angle along the flow direction of wing, whereas when the value of  $\alpha$  is less than  $-4^\circ$ , the result is opposite. The wing has a certain initial installation angle and a geometric torsion

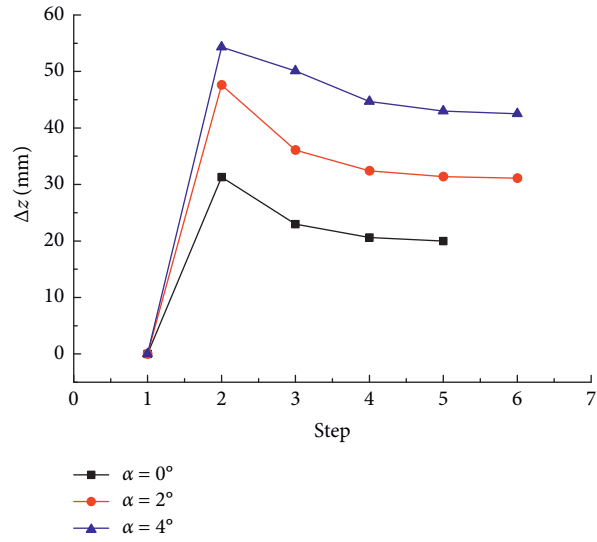


FIGURE 5: Iteration convergence of static aeroelastic deformation.

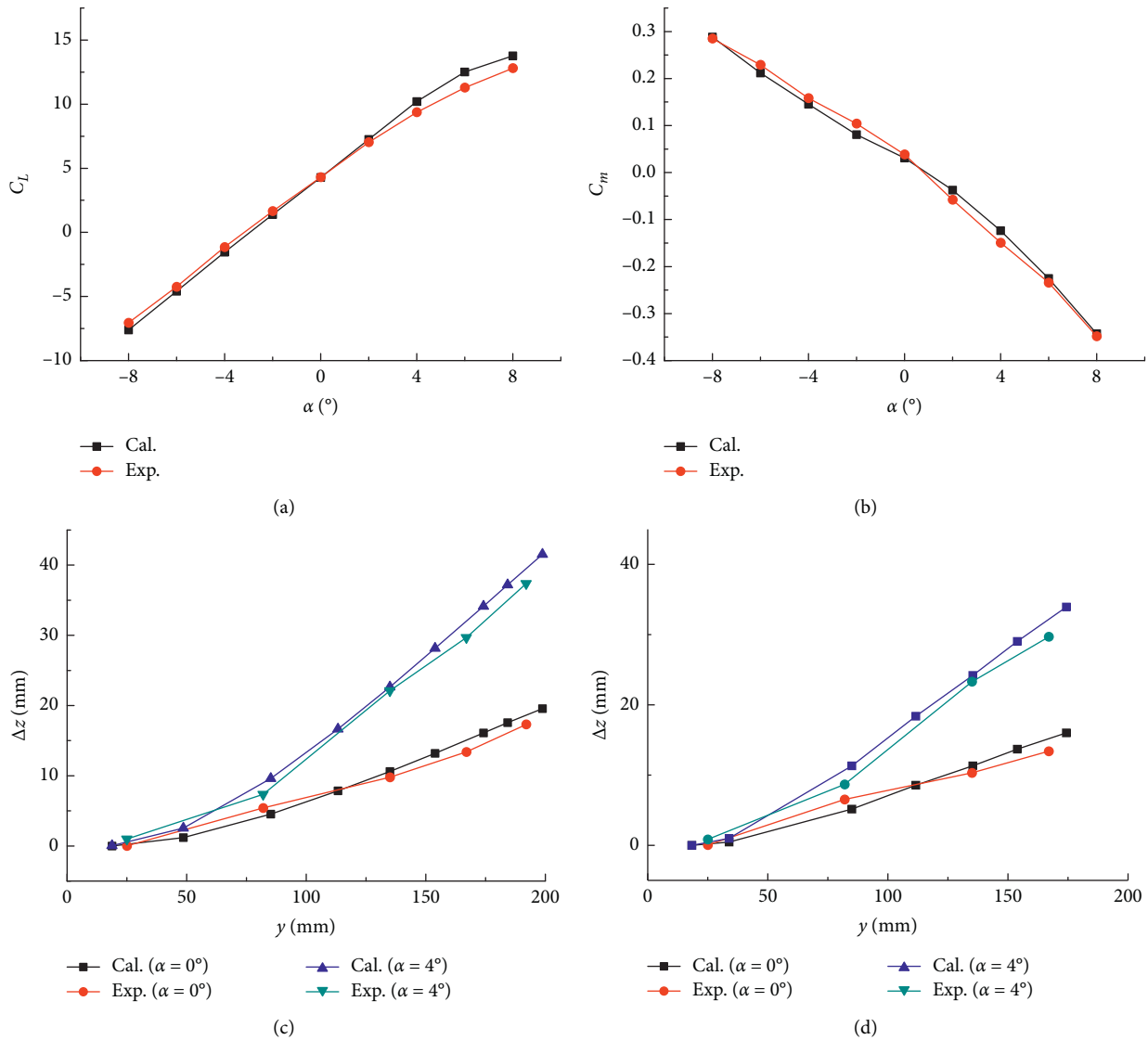


FIGURE 6: Comparison between numerical computation and wind tunnel test. (a)  $C_L \sim \alpha$ . (b)  $C_m \sim \alpha$ . (c)  $\Delta z \sim \alpha$  (front wing). (d)  $\Delta z \sim \alpha$  (rear wing).

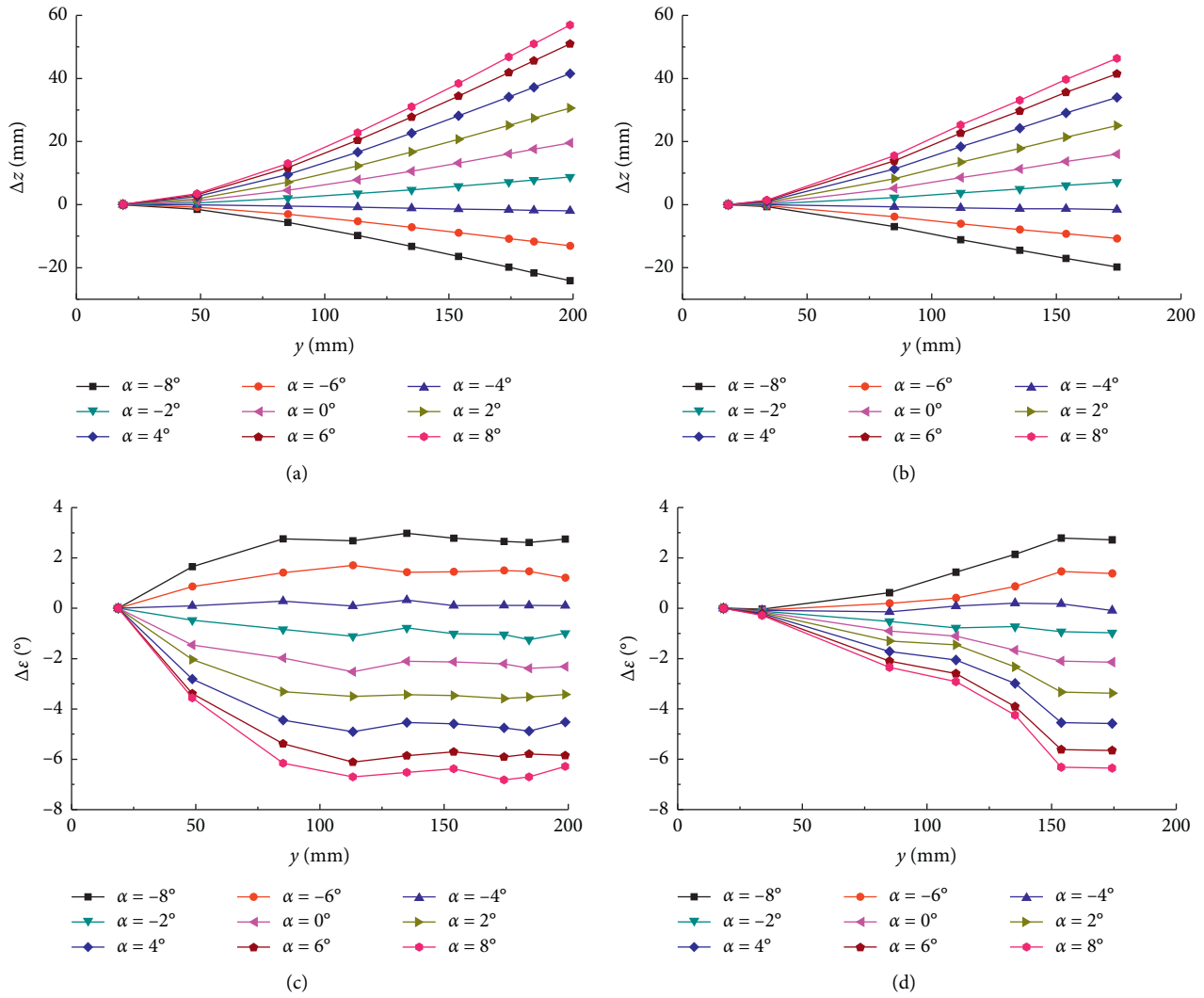


FIGURE 7: Geometry deformation characteristics of wing. (a)  $\Delta z \sim \alpha$  (front wing). (b)  $\Delta z \sim \alpha$  (rear wing). (c)  $\Delta \varepsilon \sim \alpha$  (front wing). (d)  $\Delta \varepsilon \sim \alpha$  (rear wing).

angle. The changing law corresponds to the aerodynamic load and the gradual decrease of the wing stiffness along the spanwise direction along the span. Its zero-lift angle of attack appears when the value of  $\alpha$  is about  $-4^\circ$ . It can also be seen from Figure 7 that, according to the calculation results in this paper, when  $\alpha = 4$ , the bending deformation of the front wing tip can reach 23% of the half span of the front wing, and the downstream elastic torsional deformation of the front wing tip profile can reach  $-4.5^\circ$ .

**4.2. Effect of Surface Flow Pattern.** The surface pressure coefficient of cloud chart and flow spectrum of the body near the projective wing for rigid and elastic wings are shown in Figure 8 when  $Ma = 0.8$ ,  $H = 0$  km, and  $\alpha = -4^\circ$ ,  $0^\circ$ , and  $4^\circ$ . Corresponding to the geometric deformation characteristics of the whole projectile body, the static aeroelasticity has little influence on the surface pressure and flow characteristics of the projectile body under different angles of attack. And, there is almost no difference between rigidity and elasticity.

The main reason is that the projective wing is greatly affected, especially at a high angle of attack. The specific analysis is as follows: when  $\alpha = -4^\circ$ , the lift force generated by the wing is close to zero, and the geometric deformation is small. The surface flow of rigid and elastic wings is very uniform, and the change characteristics are similar. The pressure recovery is realized in the form of a series of compression waves, and the flow presents a typical attached flow pattern. The pressure distribution on the upper surface of the wing is similar, and the aerodynamic characteristics of the rigid and elastic projective body are similar. When  $\alpha = 0^\circ$ , there is no obvious shock wave and separation stall phenomenon on the rigid wing while the effective angle of attack of the elastic wing is reduced due to the static aeroelastic effect. Accordingly, the peak negative pressure and the negative pressure range on the upper surface of the elastic wing are also significantly reduced, so is the corresponding aerodynamic load. When  $\alpha = 4^\circ$ , the peak negative pressure on the upper surface of the rigid wing is greatly enhanced, and separation and reattachment are formed along the flow

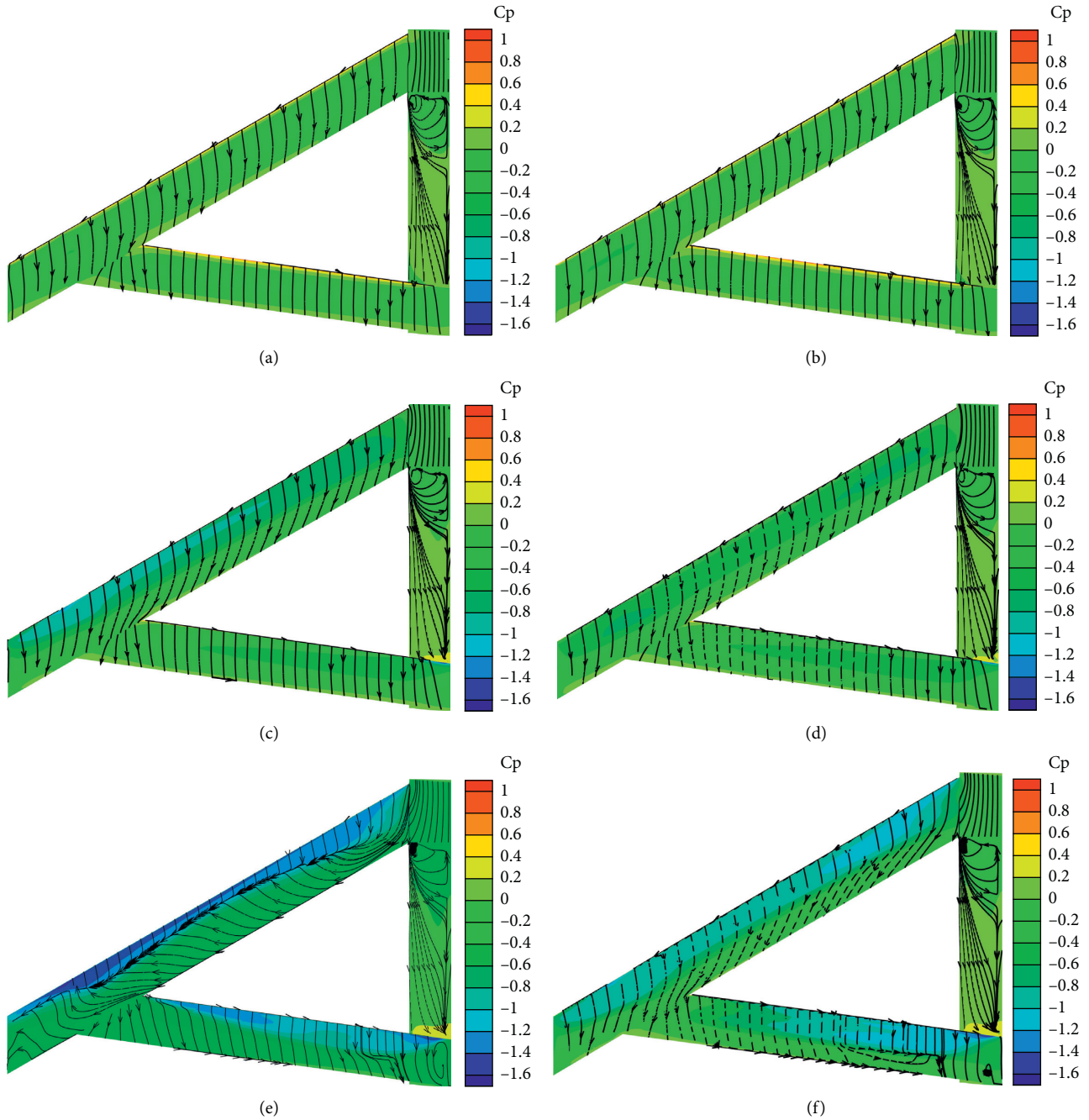


FIGURE 8: Effects of static aeroelasticity on wing surface pressure. (a) Rigid wing ( $\alpha = -4^\circ$ ). (b) Flexible wing ( $\alpha = -4^\circ$ ). (c) Rigid wing ( $\alpha = 0^\circ$ ). (d) Flexible wing ( $\alpha = 0^\circ$ ). (e) Rigid wing ( $\alpha = 4^\circ$ ). (f) Flexible wing ( $\alpha = 4^\circ$ ).

direction. By contrast, the elastic wing does not have the similar phenomenon and still maintains the attached flow pattern. A weak shock wave appears on the upper surface of the wing near the projective body, and it leads to a slight deflection of the surface streamline. With the increasing attack angle, the shock intensity on the upper surface of the rigid wing will increase, which will induce a large range of flow separation. As for elastic wing, due to the static aeroelastic effect, the effective angle of attack will decline, and the shock intensity as well as the stall separation range will be reduced. Therefore, in the range of high attack angle,

the static aeroelasticity will delay the stall separation characteristics of projective wings.

**4.3. Effect of Aerodynamic Performance.** The elastic curves and rigid curves for  $C_L \sim \alpha$ ,  $C_L \sim C_D$ , and  $L/D \sim \alpha$  of the whole bomb are shown in Figure 9 when  $Ma = 0.8$ ,  $H = 0$  km, and  $\alpha \in [-8^\circ \sim 8^\circ]$ . It can be observed that the difference of aerodynamic characteristics between rigid and elastic bomb is quite obvious owing to the static aeroelastic effect. As the aerodynamic load increases, the static aeroelasticity exerts a great influence on the aerodynamic force.

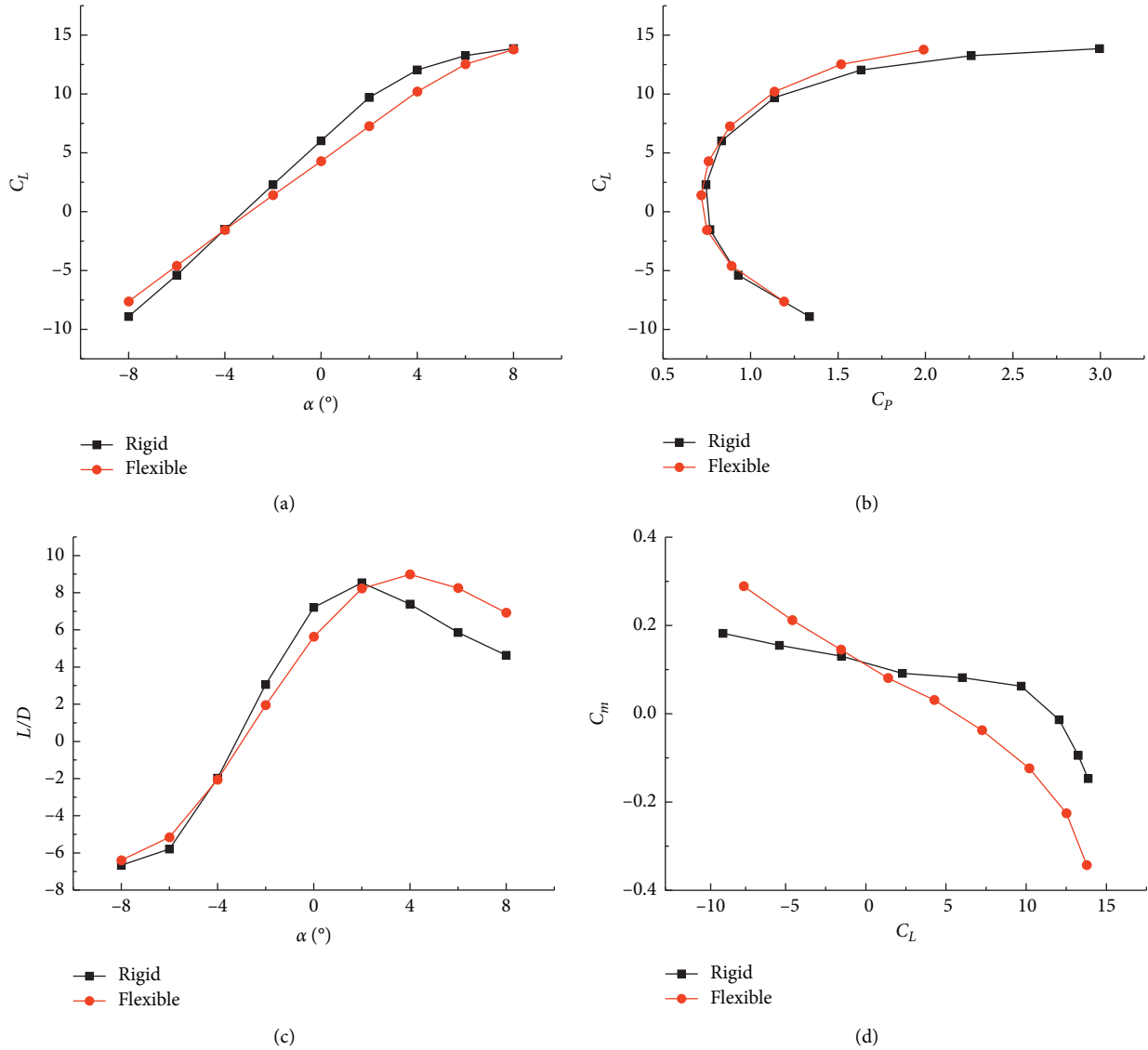


FIGURE 9: Effects of static aeroelasticity on bomb's aerodynamic characteristics. (a)  $C_L \sim \alpha$ . (b)  $C_L \sim C_D$ . (c)  $L/D \sim \alpha$ . (d)  $C_m \sim C_L$ .

Specifically, the static aeroelastic effect reduces the line slope of lift force  $C_{L\alpha}$  and the drag force, while the angle of attack related to the maximum lift drag ratio ( $L/D$ ) increases.

Additionally, under the static aeroelastic effect, the whole projectile focus moves backward, resulting in the enhancement of longitudinal static stability. The result is consistent with the geometric deformation and surface flow pattern of the projective wing. From the geometric deformation characteristics, it can be found that the static aeroelastic effect not only causes significant bending deformation of the wing but also produces torsion deformation which makes the wing to unload. Therefore, the line slope of lift force and drag force of the whole bomb will be reduced. Moreover, the static aeroelasticity delays the stall separation

of the wing, which further delays the inflection point of the lift moment curve and the angle of attack corresponding to the maximum lift-drag ratio.

According to our calculation example, compared with the rigid projectile, the slope of lift line ( $C_{L\alpha}$ ) decreases by 21% on the same angle of attack, the maximum lift drag ratio ( $L/D$ ) increases from  $2^\circ$  to  $4^\circ$ , and the focus  $X_F$  moves backward by 1.5% of the body length. The adverse effect of static aeroelasticity on its aerodynamic characteristics is mainly reflected in the deviation of cruise flight state from the design point. For a given bomb mass, if the bomb is rigid, the angle of attack will be  $0^\circ$  so as to satisfy the requirements of lift force. In terms of an elastic bomb, the angle will be about  $1^\circ$ . The cruise aerodynamic efficiency will be signifi-

cantly reduced and the total glide range will be shortened.

## 5. Conclusions

The paper studies the static aeroelastic characteristics of a SDB diamond back projective wing based on RANS equation and the coupling of CFD and CSD methods. The effectiveness of the method is verified by wind tunnel test results. The static aeroelastic effect causes the bending deformation of the front and rear wings to increase gradually along the spanwise direction and also causes the torsion deformation to the wing which is favorable to the unloading of the wing. When the angle of attack  $\alpha$  is  $4^\circ$ , the bending deformation at the tip of the wing can reach 23% of the half-span length of the wing, and the torsion deformation along the flow direction reaches  $-4.5^\circ$ . At a high angle of attack, the static aeroelasticity will delay the stall separation characteristics of the wing. Compared with the rigid projectile, the lift line slope  $C_{L\alpha}$  decreases by 21% and the focus  $X_F$  is moved backward by 1.5% of the body length. These will cause the cruise flight to deviate from the design point, thereby reducing the cruise aerodynamic efficiency and the total glide range.

## Data Availability

No data were used to support this study.

## Conflicts of Interest

The authors declare no potential conflicts of interest with respect to the research, authorship, and/or publication of this article.

## Acknowledgments

This work was funded by the Science, Technology and Innovation Commission of Shenzhen Municipality (Grant no. JCYJ20190806153615091) and project of Shaanxi Key Laboratory of Mine Electromechanical Equipment Intelligent Monitoring in Xi'an University of Science and Technology (no. SKL-MEEIM201902).

## References

- [1] J. Chen, Z. Wang, L. Zhang et al., "Numerical simulation for influence of vertical height difference to aerodynamic characteristics of diamond back wing," *Journal of Projectiles, Rockets, Missiles and Guidance*, vol. 35, no. 2, pp. 109–113, 2015, (in Chinese).
- [2] M. Sayed, T. Lutz, E. Kramer et al., "High fidelity CFD-CSD aeroelastic analysis of slender bladed horizontal-axis wind turbine," *Journal of Physics: Conference Series*, vol. 753, no. 4, p. 13, Article ID 042009, 2016.
- [3] P. A. Inthra, "Full vehicle simulations for a coaxial rotorcraft using high-fidelity CFD/CSD coupling," in *Proceedings of the AIAA Aerospace Sciences Meeting*, Kissimmee, FL, USA, January 2018.
- [4] H. Cho, S. J. Shin, and H. S. Joo, "Computational approach for vertical launcher by coupled cfd/csd with hybrid particle level-set method," in *Proceedings of the Structural Dynamics, and Materials Conference*, Grapevine, TX, USA, January 2017.
- [5] Z.-Q. Lu, K.-K. Zhang, H. Ding, and L.-Q. Chen, "Nonlinear vibration effects on the fatigue life of fluid-conveying pipes composed of axially functionally graded materials," *Nonlinear Dynamics*, vol. 100, no. 2, pp. 1091–1104, 2020.
- [6] Z. Q. Lu, D. H. Gu, H. Ding, W. Lacarbonara, and L. Q. Chen, "Nonlinear vibration isolation via a circular ring," *Mechanical Systems and Signal Processing*, vol. 136, Article ID 106490, 2020.
- [7] R. Prasad, S. Choi, D. Im, and D. Lee, "Spectral formulation-based fsi and coupled sensitivity analysis for dynamic aeroelastic problems," in *Proceedings of the 33rd AIAA Applied Aerodynamics Conference*, Dallas, TX, USA, June 2015.
- [8] J. Allan, A. Lyrio, J. L. Azevedo, D. A. Rade, and G. D. Silva, "Computational static aeroelastic analyses in transonic flows," in *Proceedings of the AIAA AVIATION 2020 FORUM*, June 2020.
- [9] Z.-Q. Lu, D. Wu, H. Ding, and L.-Q. Chen, "Vibration isolation and energy harvesting integrated in a Stewart platform with high static and low dynamic stiffness," *Applied Mathematical Modelling*, vol. 89, pp. 249–267, 2021.
- [10] Z. Q. Lu, K. K. Zhang, H. Ding, and L. Q. Chen, "Internal resonance and stress distribution of pipes conveying fluid in supercritical regime," *International Journal of Mechanical Sciences*, vol. 186, Article ID 105900, 2020.
- [11] C. Yang, L. Yang, and C. Xie, "Development of aerodynamic methods in aeroelastic analysis for high aspect ratio flexible wings," *Acta Aerodynamica Sinica*, vol. 36, no. 6, pp. 1009–1018, 2018, (in Chinese).
- [12] P. Bekemeyer and S. Timme, "Reduced order transonic aeroelastic gust response simulation of large aircraft," in *Proceedings of the 35th AIAA Applied Aerodynamics Conference*, Denver, CO, USA, June 2017.
- [13] J. Huang, Z. Zhou, H. Liu, Z. Gao, and G. Li, "Numeric simulation of aircraft gust response considering aeroelastic deformation," in *Proceedings of the 21st AIAA International Space Planes and Hypersonics Technologies Conference*, Xiamen, China, March 2017.
- [14] R. Cavallaro and L. Demasi, "Challenges, ideas, and innovations of joined-wing configurations: a concept from the past, an opportunity for the future," *Progress in Aerospace Sciences*, vol. 87, pp. 1–93, 2016.
- [15] C. Zhang, Z. Zhou, X. Zhu, and P. Meng, "Nonlinear static aeroelastic and trim analysis of highly flexible joined-wing aircraft," *AIAA Journal*, vol. 56, no. 12, pp. 4988–4999, 2018.
- [16] Z. Sotoudeh, "For challenges in the design of joined wings special session: comparison of aeroelastic stability of conventional and joined-wing highly flexible aircraft," in *Proceedings of the 56th AIAA/ASCE/AHS/ASC Structures, Structural Dynamics, and Materials Conference*, Kissimmee, Florida, January 2015.
- [17] D. Luciano, G. Monegato, and R. Cavallaro, "Minimum induced drag theorems for multi-wing systems," in *Proceedings of the 57th AIAA/ASCE/AHS/ASC Structures, Structural Dynamics, and Materials Conference*, San Diego, CA, USA, January 2016.
- [18] X. Wu, J. Lei, and J. Wu, "Numerical simulation for aerodynamic characteristics of diamond back wing," *Acta Armamentarii*, vol. 31, no. 8, pp. 1048–1052, 2010, (in Chinese).
- [19] T. Han and X. Lian, "Design of improved diamond wing in glide bomb," *Journal of Projectiles, Rockets, Missiles and Guidance*, vol. 30, no. 2, pp. 190–194, 2010, (in Chinese).

- [20] L. Demasi, E. Santarpia, A. Dipace, R. Cavallaro, and R. E. Gordnier, "Aerodynamic and structural studies of a flapping wing in forward flight," *AIAA Journal*, vol. 54, no. 9, pp. 2768–2781, 2016.
- [21] N. Teunisse, P. Tiso, L. Demasi, and R. Cavallaro, "Reduced order methods for structurally nonlinear joined wings," in *AIAA SciTech >56th AIAA/ASCE/AHS/ASC Structures, Structural Dynamics, and Materials Conference*, Kissimmee, FL, USA, January 2015.
- [22] L. Demasi, R. Cavallaro, and F. Bertucelli, "Post-critical analysis of highly deformable joined wings: the concept of snap-divergence as a characterization of the instability," *Journal of Fluids and Structures*, vol. 54, pp. 701–718, 2015.
- [23] Z. Xu, J. Wu, and X. Xue, "Structural optimization of the diamond back wing of cruise missile," *Machine Design & Research*, vol. 27, no. 1, pp. 87–90, 2010, (in Chinese).
- [24] J. Zhang, "Study on the interpolation method to calculate the aircraft wing aerodynamic pressure distribution on FEM nodes," *Aeronautical Science & Technology*, vol. 28, no. 12, pp. 14–18, 2017, (in Chinese).
- [25] F. R. Menter, R. B. Langtry, S. R. Likki, Y. B. Suzen, P. G. Huang, and S. Volker, "A correlation-based transition model using local variables part ii-test cases and industrial applications," in *Proceedings of the ASME Turbo Expo 2004: Power for Land, Sea, and Air*, Vienna, Austria, June 2004.
- [26] M. E. Biancolini, U. Cella, C. Groth et al., "Static aeroelastic analysis of an aircraft wind-tunnel model by means of modal RBF mesh updating," *Journal of Aerospace Engineering*, vol. 29, no. 6, p. 14, Article ID 04016061, 2016.
- [27] W. Liu, C. Huang, and G. Yang, "Time efficient aeroelastic simulations based on radial basis functions," *Journal of Computational Physics*, vol. 330, pp. 810–827, 2017.
- [28] H. Guo, D. Chen, and C. Zhang, "Numerical applications on transonic static aeroelasticity based on CFD/CSD method," *Acta Aerodynamica Sinica*, vol. 36, no. 1, pp. 12–16, 2018, (in Chinese).
- [29] H. Guo, G. Li, D. Chen, and B. Lu, "Numerical simulation research on the transonic aeroelasticity of a high-aspect-ratio wing," *International Journal of Heat and Technology*, vol. 33, no. 4, pp. 173–180, 2015.
- [30] P. Guo and J. Xie, "Two-dimensional CFD modeling of hysteresis behavior of MR dampers," *Shock and Vibration*, vol. 2019, Article ID 9383047, 14 pages, 2019.
- [31] J. Zornl and R. L. Davis, "3D aeroelastic simulation of flow over a solid airfoil," in *Proceedings of the 2018 Applied Aerodynamics Conference*, Atlanta, GA, USA, June 2018.
- [32] V. Joshi, R. Jaiman, G. Li, K. Breuer, and S. Swartz, "Full-scale aeroelastic simulations of hovering bat flight," in *Proceedings of the AIAA Scitech 2020 Forum*, Orlando, FL, USA, January 2020.
- [33] X. Wang, Z. Wan, and C. Yang, "A method of static aeroelastic analysis based on three dimension aerodynamic force and aeroelastic correction for hypersonic vehicles," in *Proceedings of the 55th AIAA Aerospace Sciences Meeting*, Grapevine, TX, USA, January 2017.